Calculation Method of Coupling Coefficient for Circular Coils with Bilateral Double-Layer Bounded Magnetic Shielding

Pengjie GUI, Zhiyuan LIN, and Zhongqi LI

***Abstract*—The calculation of coupling coefficient between coils is crucial for optimizing the efficiency of wireless power transfer (WPT) systems. For bilateral double-layer bounded magnetic shielding circular coils under horizontal displacement conditions, the accurate calculation of coupling coefficients currently relies mainly on time-consuming large-scale finite element simulations. To address this problem, the coupling model is divided into subregions using boundary conditions, the magnetic vector potential in each region is solved through Maxwell's equations, and a formula for the coupling coefficient of coaxial double-layer bounded magnetically shielded circular coils is derived. Additionally, a double-layer boundary vector-equivalence method is proposed, and the coupling coefficient formula for a circular coil with bilateral double-layer bounded magnetic shielding under horizontal offset is derived using spatial geometric relationships. The reliability of the proposed method is corroborated by the calculated, simulated, and laboratory-obtained values. The errors between calculated and simulated values are not more than 3.95%, and between calculated and laboratory-obtained values are not more than 4.51%, which confirms the accuracy of the proposed method. Furthermore, a significant computational speed advantage is demonstrated by the proposed method compared to simulation.**

***Index Terms*—Coupling coefficients, magnetic vector potential, vector boundary formulation, wireless power transfer.**

I. Introduction

WIRELESS power transfer (WPT) technology has emerged as a disruptive innovation in power electronics, enabling contactless energy transmission through electromagnetic coupling. This breakthrough addresses spatial constraints inherent in conventional wired systems while demonstrating superior performance in operational convenience, deployment flexibility, transmission reliability, and safety assurance. WPT systems have been widely implemented in transportation (electric vehicle charging), aerospace (satellite power systems), medical devices (implantable electronics), and underwater power applications (submarine equipment)[1]–[14]. The expanding applications of WPT technology, particularly in industrial and consumer electronics, have led to the development of diverse system architectures with varying power levels and transmission distances. Multilayer magnetic shielding, which provides superior eddy current suppression compared to single-layer designs, is typically employed to enhance electromagnetic shielding performance and improve coupling capability in WPT systems for different applications. In practical implementations, coil horizontal offset inevitably occurs due to installation tolerances or operational movements. Therefore, developing accurate calculation methods for coupling coefficients in bilateral multilayer shielded circular coils under horizontal offset is crucial for WPT systems, as it directly impacts system efficiency optimization and stability control. These calculation methods serve as fundamental tools for designing high-performance WPT systems with robust misalignment tolerance.

The current coupling coefficient calculation relies on precise mutual inductance estimation. Global research efforts have yielded diverse computational approaches for determining circular coil coupling parameters. When neither the receiver nor the transmitter has magnetic shielding, [15] and [16] apply the Biot-Savart law to compute the mutual inductance under arbitrary coil displacements. This is achieved by calculating the magnetic flux density and performing numerical integration. [17] and [18] propose an elliptic integration computational approach for determining inductive coupling between spatially misaligned circular coils, enhancing both computational speed and accuracy. [19] employs Euler angles to compute the magnetic coupling coefficient between two planar helical coils in arbitrary spatial configurations.

Incorporating magnetic shielding into the coil improves system coupling and reduces interference. For mutual inductance calculation with magnetic shielding, [20] proposed an analytical method using Fourier-Bessel expansion. It derives the mutual

Manuscript received April 21, 2025; revised July 22, 2025; accepted August 19, 2025. Date of publication December 30, 2025; date of current version September 9, 2025. This work was supported in part by Excellent Youth Project of Scientific Research of Hunan Provincial Department of Education under the grant 22B0577, Key Projects of Hunan Provincial Department of Education under the grant 23A0432, National Key R&D Program Project under the grant 2022YFB3403200, National Natural Science Foundation of China (NSFC) Youth Science Fund Project under the grant 62303178, Scientific Research Fund of Hunan Provincial Education Department under the grant 23C0182, and the Natural Science Foundation of Hunan Province under Grants under the grant 2022JJ30226. (*Corresponding author: Zhongqi Li.*)

P. Gui and Z. Lin are both with the School of Transportation and Electrical Engineering, Hunan University of Technology, Zhuzhou 412007, China (e-mail: 2284087484@qq.com; linzhiyuan 19@163.com).

Zhongqi Li is with the School of Transportation and Electrical Engineering, Hunan University of Technology, Zhuzhou 412007, China (e-mail: lizhongqi@hnu.edu.cn).

Digital Object Identifier 10.24295/CPSSTPEA.2025.00031

inductance expression for coaxial and horizontally offset circular coils, assuming the shielding material has infinite extent. [21] derived mutual inductance formulas for double-layer shielded circular coils in arbitrary positions using electric field strength and coordinate transformation. However, the assumption of infinite shielding extent in the horizontal plane limits practical applicability. For bounded magnetic shielding, [22]–[24] developed a truncated region eigenfunction expansion method to compute mutual inductance, expressing it in terms of magnetic vector potential. However, these studies only consider shielding on one side. [25] established a geometric-to-inductance mapping for bilateral bounded shielding coils using magnetic reluctance theory but was limited to coaxial configurations without addressing horizontal offsets. [26] and [27] simplify calculations using a core-less equivalent circuit, but only consider single-layer magnetic media. Similarly, although [28] derives the coupling coefficient under horizontal displacement, its theory is still limited to single-layer media and does not address the modeling of actual multi-layer shielding structures. In summary, for the bilateral multi-layer bounded magnetic shielding circular coil model, this paper proposes a more practical method for calculating the coupling coefficient of two layers.

A coupling model for bilateral double-layer bounded mag-netically shielded circular coils with horizontal offset is established in this paper. First, the model is partitioned into subregions using boundary conditions. The coaxial coupling coefficient is then derived by solving the magnetic vector potential of each subregion via Maxwell's equations. Second, a double-layer boundary vector equivalence method is proposed, and the horizontal-offset coupling coefficient is derived through spatial geometry analysis. Finally, the method is validated through numerical computation, finite-element simulation, and experimental measurement.

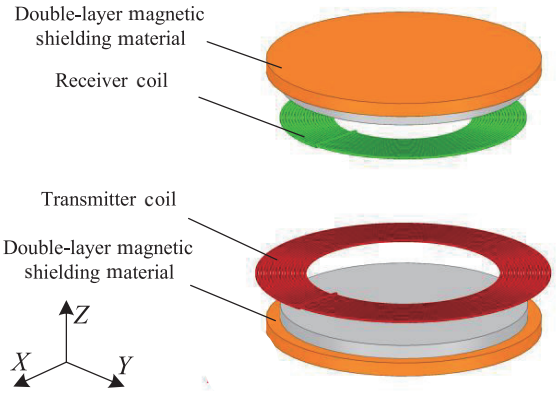

Fig. 1. 3D structure of a circular coil with double-layer magnetic shielding.

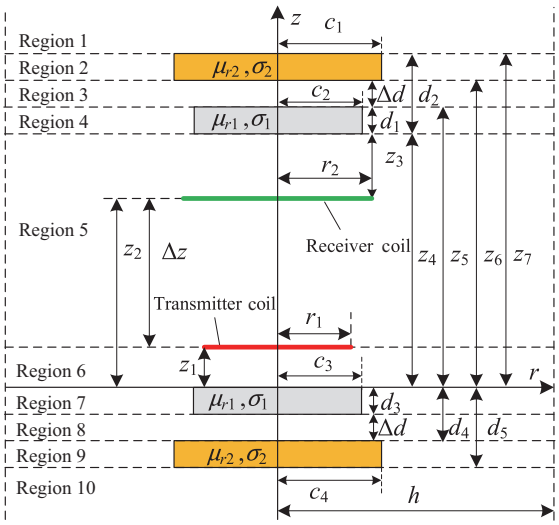

Fig. 2. Cross-section of a circular coil with double-layer magnetic shielding.

II. Calculation of the Coupling Coefficient Between Coaxial Circular Coils

A. Calculation of the Magnetic Vector Potential in Multi-Region Systems

To improve magnetic shielding performance and accommodate various application requirements, a circular coil with bilateral double-layer bounded magnetic shielding is proposed for the wireless energy transmission structure, as illustrated in Fig. 1.

Based on the cross-section of Fig. 1, Fig. 2 shows the modeled cross-section of a bilateral double-layer bounded magnetically shielded circular coil. The model divides into ten distinct regions bounded sequentially by planes at $z = -d_5$, $z = -d_4$, $z = -d_3$, $z = 0$, $z = z_1$, $z = z_4$, $z = z_5$, $z = z_6$, and $z = z_7$. Δz represents the axial offset between coil centers, with r_1 and r_2 denoting the transmitter and receiver radii respectively. The shielding materials have radii c_1, c_2, c_3 and c_4 with uniform thickness, separated by an air gap Δd. The relative permeabilities μ_{r1}, μ_{r2} and conductivities σ_1, σ_2 characterize each shielding layer. h is the hypothetical truncation distance of the magnetic vector potential. The transmitter carries current $Ie^{j\omega t}$, with amplitude I, angular frequency ω and time variation t.

Since both the magnetic shielding material and the coil in this transmission model are circular, this transmission structure has symmetry. Therefore, the magnetic vector potential $\boldsymbol{A}$ has only one component, and the direction of this component is uniformly distributed. Consequently, The electromagnetic field equations formulated in terms of the vector potential $\boldsymbol{A}$ can be simplified:

$$\nabla^2 \boldsymbol{A} = \frac{\partial^2 \boldsymbol{A}}{\partial r^2} + \frac{\partial \boldsymbol{A}}{\partial r}\frac{1}{r} + \frac{\partial^2 \boldsymbol{A}}{\partial z^2} - \frac{\boldsymbol{A}}{r^2} = -\mu J^2 \tag{1}$$

where ∇^2 is the Laplace operator, μ denotes the permeability, and J is the current density. Applying separation of variables to (1) yields the magnetic vector potential $A(r, z)$ satisfying:

$$\boldsymbol{A}(r,z) = \sum_{i=1}^{\infty} [A_o J_1(w_i r) + B_o Y_1(w_i r)](C_o e^{\lambda_i z} + C_o e^{\lambda_i z}) \tag{2}$$

In the above equation, A_o, B_o, C_o, and D_o denote the coefficients of each subregion, where subscript o serves as an index without physical meaning. The parameter w is the eigenvalue, satisfying $w^2 = \eta^2 - jw\mu_0\mu_r\sigma$, where μ_0 is the vacuum permea-

bility, and μ_r and σ are the relative permeability and conductivity of the shielding material. Here, J_1 ($w_i r$) and $Y_1(w_i r)$ represent the first-order Bessel functions J_1 and Y_1 (of the first and second kind, respectively), with i ranging from 1 to ∞ .

Since the magnetic vector potential must maintain finite values, while Y_1 ($w_i r$) diverges at the origin ($r \to 0$), to ensure convergence, the radial magnetic flux density B_s vanishes in regions 1, 3, 5, 6, 8, and 10, where the magnetic vector potential $\boldsymbol{A}(r, z)$ in these regions takes the form:

$$\boldsymbol{A}_1(r,z)=\sum_{i=1}^{\infty} J_1(w_i r) D_1 e^{-w_i z} \tag{3}$$

$$\boldsymbol{A}_3(r,z)=\sum_{i=1}^{\infty} J_1(w_i r)\left(C_3 e^{w_i z}+D_3 e^{-w_i z}\right) \tag{4}$$

$$\boldsymbol{A}_5(r,z)=\sum_{i=1}^{\infty} J_1(w_i r)\left(C_5 e^{w_i z}+D_5 e^{-w_i z}\right) \tag{5}$$

$$\boldsymbol{A}_6(r,z)=\sum_{i=1}^{\infty} J_1(w_i r)\left(C_6 e^{w_i z}+D_6 e^{-w_i z}\right) \tag{6}$$

$$\boldsymbol{A}_8(r,z)=\sum_{i=1}^{\infty} J_1(w_i r)\left(C_8 e^{w_i z}+D_8 e^{-w_i z}\right) \tag{7}$$

$$\boldsymbol{A}_{10}(r,z)=\sum_{i=1}^{\infty} J_1(w_i r) C_{10} e^{w_i z} \tag{8}$$

For eigenvalues w in (3)–(8), that can be determined by imposing the boundary condition that $\boldsymbol{A}$ is zero at the truncation boundary h. The eigenvalues are obtained when the non-exponential component vanishes at the boundary h. Consequently, the magnetic vector potential vanishes when J_1 ($w_i h$) is 0, where J_1 denotes the Bessel function of the first kind.

The inclusion of magnetic shielding materials in regions 2, 4, 7, and 9 introduces additional complexity to the boundary conditions. The domain partitions into air-filled regions and magnetic shielding material regions, where the solution in each subdomain can be expressed using boundary conditions and convergent Bessel function expansions:

$$\boldsymbol{A}_2^{\mathrm{al}}(r,z)=\sum_{i=1}^{\infty} J_1(x_i r)\left(C_2 e^{s_i z}+D_2 e^{-s_i z}\right) \tag{9}$$

$$\boldsymbol{A}_2^{\mathrm{air}}(r,z)=\sum_{i=1}^{\infty} R(s_i r)\left(C_2 e^{s_i z}+D_2 e^{-s_i z}\right) \tag{10}$$

$$\boldsymbol{A}_4^{\mathrm{fer}}(r,z)=\sum_{i=1}^{\infty} J_1(q_i r)\left(C_4 e^{p_i z}+D_4 e^{-p_i z}\right) \tag{11}$$

$$\boldsymbol{A}_4^{\mathrm{air}}(r,z)=\sum_{i=1}^{\infty} R(p_i r)\left(C_4 e^{p_i z}+D_4 e^{-p_i z}\right) \tag{12}$$

$$\boldsymbol{A}_7^{\mathrm{fer}}(r,z)=\sum_{i=1}^{\infty} J_1(q_i r)\left(C_7 e^{p_i z}+D_7 e^{-p_i z}\right) \tag{13}$$

$$\boldsymbol{A}_7^{\mathrm{air}}(r,z)=\sum_{i=1}^{\infty} R(p_i r)\left(C_7 e^{p_i z}+D_7 e^{-p_i z}\right) \tag{14}$$

$$\boldsymbol{A}_9^{\mathrm{al}}(r,z)=\sum_{i=1}^{\infty} J_1(x_i r)\left(C_9 e^{s_i z}+D_9 e^{-s_i z}\right) \tag{15}$$

$$\boldsymbol{A}_9^{\mathrm{air}}(r,z)=\sum_{i=1}^{\infty} R(s_i r)\left(C_9 e^{s_i z}+D_9 e^{-s_i z}\right) \tag{16}$$

where "al" denotes the aluminum plate material, "fer" denotes the ferrite material, and "air" denotes the air medium. q and x are the regional eigenvalues and satisfy $q^2 = p^2 - jw_i\mu_0\mu_{r1}\sigma_1$, $x^2 = s^2 - jw_i\mu_0\mu_{r2}\sigma_2$, $R(p_i r) = A_i J_1(p_i r) + B_i Y_1(p_i r)$, and $R(s_i r) = A_i J_1(s_i r) + B_i Y_1(s_i r)$, where the eigenvalues can be solved using $R(p_i h) = 0$ with $R(s_i h) = 0$.

B. Calculation of Mutual Inductance and Self-Inductance Between Circular Coils

The continuity conditions for normal and tangential components apply to the B-field and H-field of the system alike. Using this condition, the boundary conditions are satisfied as follows when the radius of the magnetic shielding material is r, taking region 2 as an example:

$$J_1(x_i c_1) = A_2 J_1(s_i c_1) + B_2 Y_1(s_i c_1) \tag{17}$$

$$\frac{1}{\mu_{r2}} x_i J_0(x_i c_1) = A_2 s_i J_0(s_i c_1) + B_2 s_i Y_0(s_i c_1) \tag{18}$$

The solution for A_2 and B_2 can be obtained by solving the simultaneous (17) and (18).

$$A_2 = \frac{s_i J_1(x_i c_1) Y_0(s_i c_1) - \frac{1}{\mu_{r2}} x_i J_0(x_i c_1) Y_1(s_i c_1)}{s_i J_1(s_i c_1) Y_0(s_i c_1) - s_i J_0(s_i c_1) Y_1(s_i c_1)} \tag{19}$$

$$B_2 = \frac{\frac{1}{\mu_{r2}} x_i J_0(x_i c_1) J_1(s_i c_1) - s_i J_0(s_i c_1) J_1(x_i c_1)}{s_i J_1(s_i c_1) Y_0(s_i c_1) - s_i J_0(s_i c_1) Y_1(s_i c_1)} \tag{20}$$

Similarly one can find the coefficients A_4, B_4, A_7, B_7, A_9, B_9 in regions 4, 7, 9. Using the boundary conditions between each neighboring region one can obtain the following:

$$\boldsymbol{A}_m(r, z_n) = \boldsymbol{A}_{m+1}(r, z_n) \tag{21}$$

$$\left.\frac{\partial \boldsymbol{A}_m(r,z)}{\partial z}\right|_{z=z_n} - \left.\frac{\partial \boldsymbol{A}_{m+1}(r,z)}{\partial z}\right|_{z=z_n} = -\mu J \tag{22}$$

Due to the presence of Bessel and Neumann functions in the proposed formula, which ensures rapid convergence, an approximation can be obtained by considering only a finite number of terms in the magnetic vector potential series. Taking (3) as an example, when i takes the first n terms, both sides of the equation are multiplied by $J_1(w_i r) \cdot r$, integrating over r from 0 to the truncated region h. Applying the orthogonality of Bessel functions yields the following simplified form:

$$\int_0^h \sum_{i=1}^{\infty} D_1 e^{-k_i z} J_1(w_i r) J_1(w_i r) r \,\mathrm{d}r = \sum_{i=1}^{\infty} \frac{h^2}{2} D_1 e^{-k_i z} J_2(w_i h) \tag{23}$$

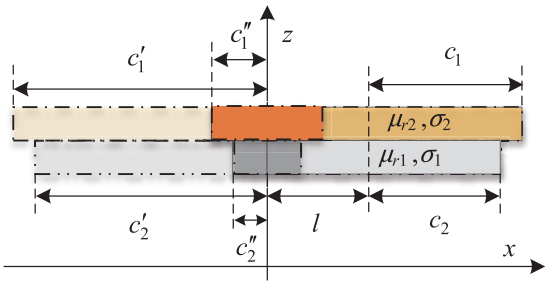

Fig. 3. Schematic cross-section of the two-layer boundary vector equivalence method after horizontal offsetting.

Similarly, the above method can be used to convert (21) and (22) into matrix form. Then, using Cramer's rule, the unknown coefficients $D_1 - D_9$ and $C_2 - C_{10}$ can be obtained. The solution process is shown in the appendix.

To determine the system's mutual inductance, only the magnetic flux through region 5 needs to be considered. The mutual inductance can then be expressed as:

$$M=\frac{2\pi r_2}{I}\sum_{i=1}^{\infty} J_1(wr_2)\left(C_5e^{uz_2}+D_5e^{-uz_2}\right) \tag{24}$$

The self-inductance parameter of the transmitting coil, L_1, and the self-inductance parameter of the receiver coil, L_2, can be calculated by considering identical coil geometries, while the mutual inductance at zero coaxial distance is derived by

$$L_1=\frac{2\pi r_1}{I}\sum_{i=1}^{\infty} J_1(wr_1)\left(C_5e^{uz_1}+D_5e^{-uz_1}\right) \tag{25}$$

$$L_2=\frac{2\pi r_2}{I}\sum_{i=1}^{\infty} J_1(wr_2)\left(C_5e^{uz_2}+D_5e^{-uz_2}\right) \tag{26}$$

The coupling coefficient k is given by (27)

$$k=\frac{M}{\sqrt{L_1\cdot L_2}} \tag{27}$$

III. Calculation of Inter-Coil Coupling Coefficient at Horizontal Offset

For horizontal offset analysis in double-layer magnetic shielding, a boundary vector equivalence method is proposed. Fig. 3 shows the cross-section after offset application, where l denotes the + x-axis offset. The initial radius of the original double-layer magnetic shielding is added and subtracted from the horizontal offset, respectively, and is equivalent to a large double-layer magnetic shielding material and a small double-layer magnetic shielding material. The radii after the equivalence are brought into the original parameters c_1 and c_2 to find the coefficients C_5 and D_5 of region 5.

In Fig. 3, the radius of the coaxial magnetic shielding material after the equivalent c_1' and c_1'', with respect to c_1, can be described by the matrix expression as follows:

$$\begin{bmatrix} c_1' \\ c_1'' \end{bmatrix}=\begin{bmatrix} 1 & -l \\ 1 & l \end{bmatrix}\begin{bmatrix} c_1 \\ 1 \end{bmatrix} \tag{28}$$

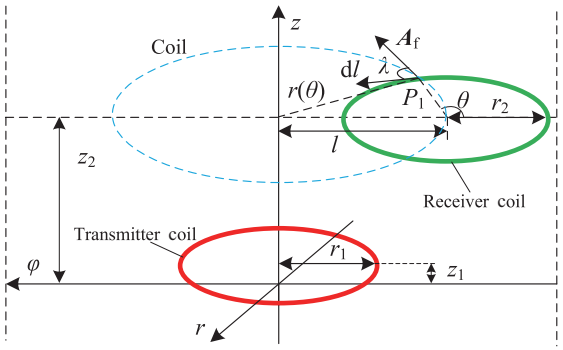

Fig. 4. Receiver coil horizontal offset 3D structural diagram.

To analyze the receiver coil's horizontal offset, Fig. 4 presents the corresponding 3D schematic. The parameter l represents the horizontal offset distance from the z-axis symmetry center. Considering point P_1 on the coil, its differential tangent vector element is denoted dl as its tangent component, and the tangent $\boldsymbol{A}_f$ of the Coil with $r(\theta)$ as the radius is the magnetic vector potential component, and the angle of both of them is λ.

The parametric equations of the receiver coil and coil are established separately as follows:

$$\begin{cases} x_c = r_2\cos\theta \\ y_c = r_2\sin\theta \\ z_c = z_2 \end{cases} \tag{29}$$

$$\begin{cases} x_o = r(\theta)\cos\varphi \\ y_o = r(\theta)\sin\varphi \\ z_o = z_2 \end{cases} \tag{30}$$

When offsetting the receiver coil alters its relative position, the following relationships hold

$$\begin{bmatrix} x_n \\ y_n \\ z_n \end{bmatrix}=\begin{bmatrix} x_c \\ y_c \\ z_c \end{bmatrix}+\begin{bmatrix} l \\ 0 \\ 0 \end{bmatrix} \tag{31}$$

Based on the geometric relationships

$$r(\theta)=\sqrt{x_2^2+y_2^2} \tag{32}$$

The corresponding tangent vectors are obtained by derivatives of θ and φ in (28) and (29), respectively.

$$\begin{cases} \alpha_1=[-r_2\sin\theta, r_2\cos\theta, 0]^{\mathrm{T}} \\ \beta_1=[-r(\theta)\sin\varphi, r(\theta)\cos\varphi, 0]^{\mathrm{T}} \end{cases} \tag{33}$$

Finally, the solution is obtained by substituting the cosine value between the two vectors into (24).

$$M=\frac{\Phi}{I}=\frac{r_2}{I}\int_0^{2\pi}\boldsymbol{A}_5[r(\theta), z_n]\frac{\alpha_1\cdot\beta_1}{|\alpha_1||\beta_1|}\mathrm{d}\theta \tag{34}$$

The horizontal offset coupling coefficient k is calculated by substituting (34), (25), and (26) into (27). Similarly, this meth-

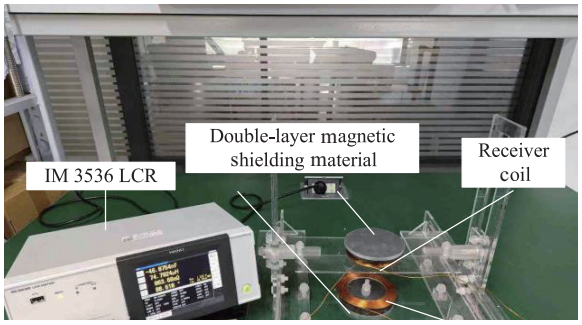

Fig. 5. Experimental setup diagram.

TABLE I
COIL AND MAGNETIC SHIELDING MATERIAL PARAMETERS

Symbol	Parameter	Value
T_1	Transmitter coil turns	17
T_2	Receiver coil turns	18
R_{t0}	Transmitter coil initial radius	35 mm
R_{r0}	Receiver coil initial radius	25 mm
ΔR	Radius change	1.1 mm
z_1	Transmitter coil height	12 mm
z_2	Receiver coil height	22–112 mm
z_3	Receiver side magnetic shielding	13 mm
c_2, c_3	Ferrite material radius	48.5 mm
c_1, c_4	Aluminum plate material radius	50 mm
d	Thickness of magnetic shielding material	5 mm
μ_{r1}	Ferrite relative permeability	2800
σ_1	Ferrite conductivity	0.01 S/m
μ_{r2}	Relative permeability of aluminum plate	1.000021
σ_2	Aluminum plate conductivity	3.8×10^7 S/m

od extends to multi-layer magnetic shielding structures of arbitrary sizes. The proposed calculation method calculates circular planar helical coils as concentric circles with different radii, so there are some minor errors.

IV. SIMULATION AND EXPERIMENTATION

To validate the proposed formula for horizontal-offset coupling coefficients in doubly-bounded magnetically shielded circular coils, simulations are performed using Ansys Maxwell, with results shown in Fig. 1. Experimental measurements use an IM3536 LCR meter at an 85 kHz operating frequency. Formula validity and computational efficiency are verified through comparative analysis of vertical/horizontal offsets and computation time. The experimental configuration appears in Fig. 5.

The mutual inductance measurement principle using an impedance analyzer is that the transmitter coil and receiver coil forward series results in L_1+L_2+2M; reverse series results in L_1+L_2-2M; and the mutual inductance M is determined by

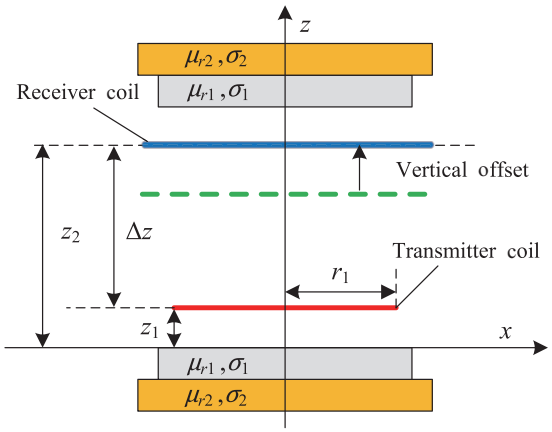

Fig. 6. Schematic of the vertical offset on the receiving side.

the following fundamental relation: $M = (L_1-L_2)/4$. Table I lists the coil and magnetic shielding parameters. For experimental consistency, all shielding materials share identical radius and thickness specifications. Given the negligible air-gap effect in practical operation, we set $\Delta d = 0$ for simulations.

For the purpose of analysis, it is necessary to define the simulation error coefficient ε_1 and the experimental error coefficient ε_2 for the coupling coefficients, as shown in (35) and (36):

$$\varepsilon_1 = \frac{|k_c - k_s|}{k_s} \times 100\% \tag{35}$$

$$\varepsilon_2 = \frac{|k_c - k_e|}{k_e} \times 100\% \tag{36}$$

where k_c, k_s, and k_e represent the calculated, simulated, and experimental coupling coefficients, respectively.

A. Vertical Offset

The receiver side magnetic shielding material and the receiver coil are collectively referred to as the receiver side in this paper, and for the receiver side vertical offset experiment, the receiver coil is set to be vertically offset from $z_2 = 22$ mm along the + z-axis to $z_2 = 112$ mm in steps of 10 mm in sequence, as shown in Fig. 6.

The vertical separation distance on the receiver side is Δz in the figure, and the dashed line is the starting position of the receiver side before the offset. The measured coupling coefficient data and error comparisons for the receiver side vertical offset are shown in Table II. The errors ε_1 of the coupling coefficients of the calculated and simulated values are not greater than 3.95%, and the errors ε_2 of the coupling coefficients of the calculated and experimental values are not greater than 4.51%. The results of the coupling coefficients of the computational results with the numerical simulations and the experimental measurements are in good agreement. Combined with Table II, the calculated, simulated, and experimental coupling coefficients with the vertical distance of the receiver side are established as shown in Fig. 7.

TABLE II
COUPLING COEFFICIENTS AND ERRORS FOR VERTICAL OFFSETS ON THE RECEIVER SIDE

Δz/mm	k_c	k_s	k_e	ε_1/%	ε_2/%
10	0.5823	0.5711	0.5782	1.97	0.71
20	0.3911	0.3796	0.3906	3.05	0.14
30	0.2615	0.2570	0.2585	1.75	1.14
40	0.1766	0.1780	0.1818	0.80	2.90
50	0.1234	0.1262	0.1266	2.26	2.56
60	0.0935	0.0915	0.0912	2.15	2.51
70	0.0651	0.0677	0.0672	3.95	3.16
80	0.0492	0.0511	0.0515	3.83	4.51
90	0.0381	0.0393	0.0388	3.08	1.91
100	0.0303	0.0307	0.0309	1.25	2.12

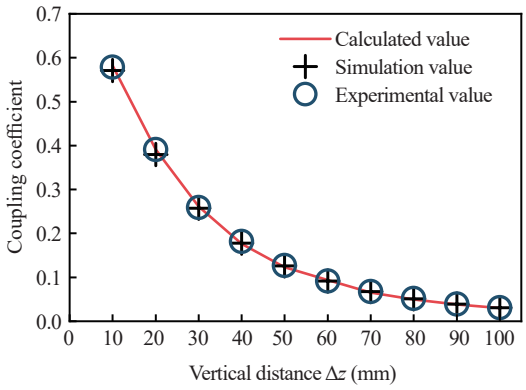

Fig. 7. Vertical offset coupling coefficient variation graph.

Analysis of Fig. 7 reveals that the coupling coefficient gradually decreases as the perpendicular distance between receiver and transmitter coils increases, because the enhanced coil separation progressively reduces their magnetic flux linkage, thereby diminishing the coupling degree.

B. Horizontal Offset

In the horizontal offset experiment on the receiver side, z_2 is set to 72 mm, and the vertical distance (Δz) between the receiver coil and the transmitting coil is 60 mm. The receiver side starts at a horizontal distance l = –50 mm and is offset along the positive x-axis in 10 mm increments up to l = 50 mm. The experimental setup is illustrated in Fig. 8. The measured coupling coefficients and their corresponding errors for horizontal offset are presented in Table III. l denotes the horizontal offset distance.

Analyzing Table III, it can be seen that the errors of both the calculated value coupling coefficients and the simulated value coupling coefficients are not greater than 3.69% at the lateral displacement of the receiver assembly. The error ε_2 between the calculated value coupling coefficient and the experimental value coupling coefficient is not more than 2.51%. The results of calculated values and simulated and experimental values

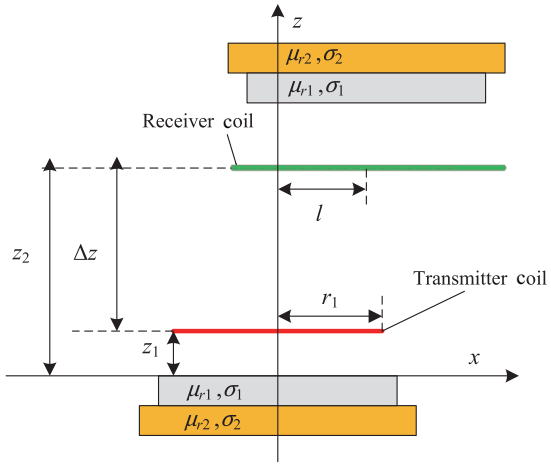

Fig. 8. Schematic diagram of horizontal offset on the receiver side.

TABLE III
COUPLING COEFFICIENTS AND ERRORS AT HORIZONTAL OFFSET ON THE RECEIVING SIDE

l/mm	k_c	k_t	k_s	ε_1/%	ε_2/%
–50	0.0411	0.0423	0.0421	2.86	2.35
–40	0.0565	0.0563	0.0563	0.32	0.25
–30	0.0724	0.0698	0.0738	3.69	1.87
–20	0.0834	0.0812	0.0837	2.69	0.31
–10	0.0916	0.0888	0.0896	3.09	2.26
0	0.0935	0.0915	0.0912	2.15	2.51
10	0.0916	0.0889	0.0903	3.05	1.46
20	0.0834	0.0813	0.0828	2.62	0.73
30	0.0724	0.0699	0.0713	3.57	1.57
40	0.0565	0.0564	0.0556	0.12	1.58
50	0.0411	0.0424	0.0410	3.07	0.25

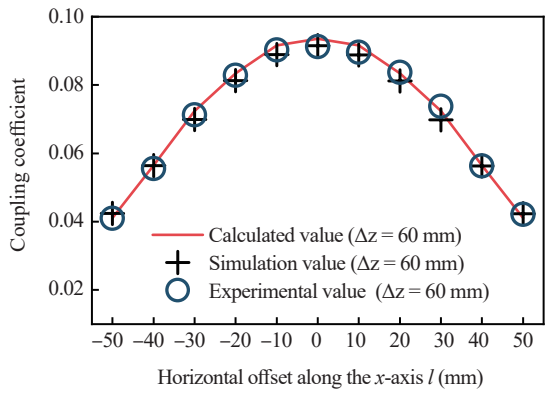

Fig. 9. Plot of variation of horizontal offset coupling coefficient at receiver side.

have good agreement at the lateral displacement of the receiver assembly. Combined with Table III, the variation curves of the coupling coefficients of the calculated, simulated, and experimental values with the horizontal offset of the receiver side are established as shown in Fig. 9.

TABLE IV
COUPLING COEFFICIENTS WHEN THE NUMBER OF TURNS OF THE RECEIVING COIL IS VARIED

N_2	k_c	k_s	k_e	ε_1/%	ε_2/%
14	0.0834	0.0828	0.0842	0.72	−0.95
15	0.0865	0.0851	0.0874	1.65	−1.03
16	0.0885	0.0872	0.0891	1.49	−0.67
17	0.0912	0.0894	0.0904	2.01	0.88
18	0.0935	0.0915	0.0938	2.19	−0.32
19	0.0955	0.0936	0.0942	2.03	1.38
20	0.0974	0.0957	0.0966	1.78	0.83
21	0.0998	0.0977	0.0969	2.15	2.99
22	0.1011	0.0997	0.0983	1.40	2.85
23	0.1045	0.1016	0.1025	2.85	1.95

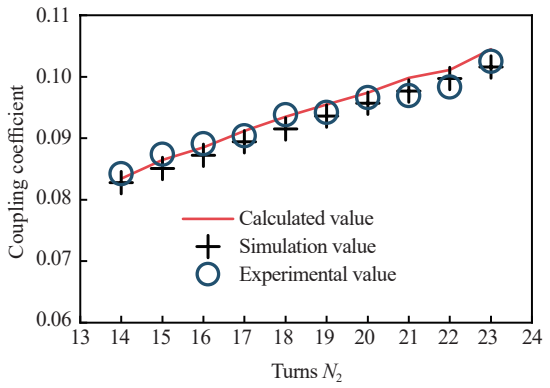

Fig. 10. Coupling coefficient curve when the number of turns of receiver coil changes.

Fig. 9 analysis reveals that at constant vertical height, as the receiver moves left or right along the *x*-axis (with *z* as central axis), the coupling coefficient decreases with increasing distance from the *z*-axis. This occurs because the structure's magnetic flux diminishes radially outward from the center, causing the coupling coefficient to decrease proportionally with horizontal offset distance.

C. Receiver Coil Turns Change

To verify the validity of the method for turn variations, only the receiver side coil turns were varied, keeping other parameters identical to Table I. The receiver side turns (N_2) increased from 14 to 23 in one-turn increments, with coupling coefficients recorded at 50 mm coaxial height, as shown in Table IV. Table IV shows that when the receiver coil turns vary from 14 to 23, the simulation error of the coupling coefficient remains no greater than 2.19% and experimental errors are not greater than 2.80%, validating the calculation method. Based on Table IV data, Fig. 10 plots the calculated, experimental, and simulated coupling coefficients versus turn count varia- tions.

TABLE V
COUPLING COEFFICIENTS WHEN THE NUMBER OF TURNS OF THE RECEIVER COIL IS VARIED

Δz/mm	t_a/s	t_b/s	l/mm	t_c/s	t_d/s	N_2	t_a/s	t_b/s
10	300	2.7777	−50	268	2.3827	14	209	2.2645
20	294	2.7737	−40	278	2.9921	15	230	2.2832
30	295	2.8111	−30	287	2.8100	16	254	2.3711
40	278	2.8956	−20	284	2.9646	17	278	2.4647
50	266	2.6279	−10	266	2.9646	18	304	2.5044
60	282	2.8171	0	304	2.7282	19	326	2.6362
70	304	2.8262	10	258	2.8922	20	361	2.6656
80	309	2.7725	20	286	2.6042	21	387	2.7422
90	286	2.7689	30	271	2.6494	22	401	2.8163
100	288	2.7952	40	282	2.5862	23	424	2.8940
110	281	2.7235	50	266	2.2565	24	440	2.9630

D. Comparison of Computation and Simulation Speed

This paper proposes an integrated computational model for systematically comparing the performance between Matlab programs and Ansys Maxwell simulations in electromagnetic system analysis. The study focuses on evaluating the coupling coefficients of bilateral double-layer magnetically shielded horizontally offset circular coil structures. Under identical hardware conditions (excluding Maxwell's initial modeling time), rigorous tests were conducted to ensure fair comparison. As shown in Table V, significant differences in computational efficiency were observed between the two approaches. The investigation examined three key variables. vertical offset distance, horizontal offset displacement, and receiver coil turns variation. Multiple trials were performed and average computation times were recorded to ensure statistical reliability.

Table V shows the Ansys Maxwell simulation averages 289.4 s for vertical offset, compared to 2.78 s for the Matlab program. Horizontal offset simulations average 278.4 s (Maxwell) versus 2.75 s (Matlab). Per additional coil turn, Maxwell requires 20.9 s versus 0.06 s of Matlab, demonstrating our method's substantial speed advantage.

E. Comparison of Domestic and International Calculation Methods

The proposed boundary vector equivalence method achieves superior performance in horizontal offset coupling coefficient calculation, demonstrating a maximum error of 4.51%. Table VI presents comparative results with existing methods from literature.

The abbreviations and acronyms presented in the table are explicitly defined and explained as follows: DTD stands for different transmission distances, HO represents horizontal offset, FMS denotes bounded magnetic medium, DS indicates that the magnetic medium demonstrates bilateral symmetry characteristics, and ERR signifies the maximum allowable computational error percentage.

TABLE VI
COUPLING COEFFICIENTS WHEN THE NUMBER OF TURNS OF THE RECEIVING COIL IS VARIED

Literatures	Methodologies	DTD	HO	FMS	DS	ERR
[20]	The Fourier-Bessel	√	√	×	√	/
[21]	Coordinate transformation	√	√	√	×	4.78%
[23]	Truncated zoning	√	√	√	×	4.76%
[24]	Space boundary vector	√	√	√	×	3.26%
[25]	Theory of magnetic circuit	×	×	√	√	8.13%
This work	Boundary vector equivalence	√	√	√	√	4.51%

V. CONCLUSION

This paper addresses the coupling coefficient calculation for horizontally offset circular coils with bilateral double-layer bounded magnetic shielding. The model divides the coupling region into subdomains by boundary characteristics and solves the magnetic vector potential of each region using Maxwell's equations and employs a double-layer boundary vector equivalence method to calculate magnetic shielding material offsets. Combined with spatial geometric relations, this enables coupling coefficient calculation for horizontally offset coils. The validity of the method is confirmed through calculated, simulated, and experimental results. Calculation errors remain below 3.95% versus simulations and 4.51% versus experiments. These results fully validate the proposed method for horizontal-offset bilateral double-layer shielded circular coils. Speed comparisons demonstrate the significant computational advantage of the method. The formulation provides crucial theoretical support for optimizing horizontal-offset bilateral double-layer shielded coil transmission structures. It also facilitates future research on coupling coefficients for multi-layer shielded coils at arbitrary positions.

APPENDIX

Cramer's Rule Implementation: By applying the boundary condition relations given in (21) and (22), we obtain the system of equations for the unknown variables:

$$\boldsymbol{S}=\boldsymbol{U}^{-1}\cdot\boldsymbol{I} \tag{37}$$

where $\boldsymbol{U}$ is an 18×18 boundary condition matrix, $\boldsymbol{S}$ is an 18×1 column vector of unknowns, and $\boldsymbol{I}$ is an 18×1 source term column vector. Take the boundary conditions of the first region as an example:

$$\boldsymbol{A}_1(r,z)\big|_{z=z_7}=\boldsymbol{A}_2(r,z)\big|_{z=z_7} \tag{38}$$

$$\frac{\partial \boldsymbol{A}_1}{\partial z}\bigg|_{z=z_7}=\frac{\partial \boldsymbol{A}_2}{\partial z}\frac{1}{\mu_{r2}}\bigg|_{z=z_7} \tag{39}$$

The boundary conditions for regions 2 to 10 are solved in the same way. The boundary condition matrix is as follows:

$$\begin{cases}\boldsymbol{U}_1=[-Ge^{s_i z_7}\ \cdots\ 0\ \ Ee^{-w_i z_7}\ -Ge^{-s_i z_7}\ \cdots\ 0\ \ 0]\\ \boldsymbol{U}_2=[-Nse^{s_i z_7}\ \cdots\ 0\ -Ewe^{-w_i z_7}\ \ Ne^{-s_i z_7}\ \cdots\ 0\ \ 0]\\ \boldsymbol{U}_3=[Ge^{s_i z_6}\ -Ee^{w_i z_6}\ \cdots\ 0\ \ Ge^{-s_i z_6}\ \ -Ee^{-w_i z_6}\ \cdots\ 0]\\ \vdots\\ \boldsymbol{U}_{15}=[0\ \cdots\ Ee^{w_i d_4}-Ge^{s_i d_4}\ \cdots\ 0\ \ Ee^{-w_i d_4}\ \ -Ge^{-s_i d_4}]\\ \boldsymbol{U}_{16}=[0\ \cdots\ Ewe^{w_i d_4}-Nse^{s_i d_4}\ \cdots\ 0\ -Ewe^{-w_i d_4}\ Nse^{-s_i d_4}]\\ \boldsymbol{U}_{17}=[0\ \ 0\ \cdots\ Ge^{s_i d_5}\ \ -Ee^{w_i d_5}\ \ \cdots\ \ 0\ \ Ge^{-s_i d_5}]\\ \boldsymbol{U}_{18}=[0\ \ 0\ \cdots\ Nse^{s_i d_5}\ \ -Ewe^{w_i d_5}\ \cdots\ 0\ -Nse^{-s_i d_5}]\end{cases} \tag{40}$$

$$\boldsymbol{S}=[C_2\ \ C_3\ \ \cdots\ \ C_9\ \ C_{10}\ \ D_1\ \ D_2\ \ \cdots\ \ D_8\ \ D_9]^{\mathrm{T}} \tag{41}$$

$$\boldsymbol{I}=\left[0\ \ 0\ \ \cdots\ \ \frac{-\mu_0 I\delta(r-r_0)J_1(w^{\mathrm{T}}r)}{E}\cdots\ \ 0\ \ 0\right]^{\mathrm{T}} \tag{42}$$

where E, G, N, U, and V represent nth-order diagonal matrices, with the explicit expressions for E, G, and N given below, and U and V following analogously to G and N.

$$E=\int_0^h J_1(w_i r)J_1(w_j r)r\mathrm{d}r=\delta\frac{[J_0(w_i h)]^2}{2} \tag{43}$$

$$G=\int_0^c J_1(s_i r)J_1(q_j r)r\mathrm{d}r+\int_c^h J_1(s_i r)R_1(p_j r)r\mathrm{d}r \tag{44}$$

$$N=\frac{1}{\mu_r}\int_0^c J_1(s_i r)J_1(q_j r)r\mathrm{d}r+\int_c^h J_1(s_i r)R_1(p_j r)r\mathrm{d}r \tag{45}$$

ACKNOWLEDGMENTS

This work was supported in part by the Natural Science Foundation of Hunan Province under Grants 2022JJ30226, National Key R&D Program Project (2022YFB3403200), Key Projects of Hunan Provincial Department of Education (23A0432), and in part by Excellent Youth Project of Scientific Research of Hunan Provincial Department of Education (22B0577), National Natural Science Foundation of China (NSFC) Youth Science Fund Project (62303178), and A Project Supported by Scientific Research Fund of Hunan Provincial Education Department (23C0182).

REFERENCES

[1] S. Y. R. Hui, "Past, present and future trends of non-radiative wireless power transfer," in *CPSS Transactions on Power Electronics and Applications*, vol. 1, no. 1, pp. 83–91, Dec. 2016.

[2] Y. Zhang, S. Chen, X. Li, and Y. Tang, "Design of high-power static wireless power transfer via magnetic induction: An overview," in *CPSS Transactions on Power Electronics and Applications*, vol. 6, no. 4, pp. 281–297, Dec. 2021.

[3] E. Abramov, I. Zeltser, and M. M. Peretz, "A network-based approach for modeling resonant capacitive wireless power transfer systems," in *CPSS Transactions on Power Electronics and Applications*, vol. 4, no. 1, pp. 19–29, Mar. 2019.

[4] Z. Li, Z. Chen, M. Yang, Y. Cheng, X. Xiong, and S. Huang, "Design of edge-enhanced coil structure to obtain constant mutual inductance with horizontal misalignment in wireless power transfer systems of electric vehicles," in *CPSS Transactions on Power Electronics and Applications*, vol. 9, no. 2, pp. 141–151, Jun. 2024.

[5] C. Liao, J. Li, and S. Li, "Design of lcc impedance matching circuit for wireless power transfer system under rectifier load," in *CPSS*

Transactions on Power Electronics and Applications, vol. 2, no. 3, pp. 237–245, Sept. 2017.

[6] Z. Li, W. Zhang, Z. Gan, and B. Li, "Study on composite structure of tian-font magnetic shielding and anti-series active coils for wireless power transfer system," in *CPSS Transactions on Power Electronics and Applications,* vol. 10, no. 1, pp. 97–109, Mar. 2025.

[7] A. Harhouz, D. Aissaoui, A. Chaabane, and M. Benaissa, "Highly efficient wireless power transfer systems for implantable medical devices," in *Proceedings of 2024 International Conference on Telecommunications and Intelligent Systems (ICTIS)*, Dec. 2024, pp. 1–4.

[8] C. Park, J. Park, Y. Shin, J. Kim, S. Huh, D. Kim, S. Park, and S. Ahn, "Separated circular capacitive coupler for reducing cross coupling capacitance in drone wireless power transfer system," in *IEEE Transactions on Microwave Theory and Techniques*, vol. 68, no. 9, pp. 3978–3985, Sept. 2020.

[9] X. Yi, W. Zheng, H. Cao, S. Wang, X. Feng, and Z. Yang, "Wireless power transmission for implantable medical devices using focused ultrasound and a miniaturized 1-3 piezoelectric composite receiving transducer," in *IEEE Transactions on Ultrasonics, Ferroelectrics, and Frequency Control*, vol. 68, no. 12, pp. 3592–3598, Dec. 2021.

[10] Z. Cheng, Y. Lei, K. Song, and C. Zhu, "Design and loss analysis of loosely coupled transformer for an underwater high-power inductive power transfer system," in *IEEE Transactions on Magnetics*, vol. 51, no. 7, pp. 1–10, Jul. 2015.

[11] Y. Yao and M. Nekovee, "Efficiency-enhanced holographic metasurface for wireless power transfer based in electric vehicles," in *IEEE Antennas and Wireless Propagation Letters*, vol. 24, no. 2, pp. 299–303, Feb. 2025.

[12] C. Da, F. Li, M. Nie, S. Li, C. Tao, and L. Wang, "Undersea capacitive coupled simultaneous wireless power and data transfer for multiload applications," in *IEEE Transactions on Power Electronics*, vol. 40, no. 1, pp. 2630–2642, Jan. 2025.

[13] D. Ferdous, S. Saha, and R. Ray, "A resonance based inductive wireless power transfer system for charging autonomous underwater vehicle (auv) batteries," in *Proceedings of 2024 International Conference on Electrical Electronics and Computing Technologies (ICEECT)*, vol. 1, Aug. 2024, pp. 1–6.

[14] V. Ramakrishnan, D. Savio A, M. Shorfuzzaman, and W. Mohammed Abdelfattah, "An enhanced vehicle-to-vehicle wireless power transfer system for electric vehicle applications using a reconfigurable coil approach," in *IEEE Access*, vol. 13, pp. 9931–9941, 2025.

[15] E. Yıldırız and S. B. Kemer, "Novel semi-analytical method for mutual inductance calculation of the thin spiral disk coils," in *IET Electric Power Applications*, vol. 13, pp. 1607–1612, 2019. [Online]. Available: https://digital-library.theiet.org/doi/abs/10.1049/iet-epa.2019.0206

[16] K.-H. Song, J. Feng, R. Zhao, and X.-L. Wu, "A general mutual inductance formula for parallel non-coaxial circular coils," in *The Applied Computational Electromagnetics Society Journal (ACES)*, pp. 1385–1390, 2019.

[17] Y.-L. Lyu, F.-Y. Meng, G.-H. Yang, B.-J. Che, Q. Wu, L. Sun, D. Erni, and J. L.-W. Li, "A method of using nonidentical resonant coils for frequency splitting elimination in wireless power transfer," in *IEEE Transactions on Power Electronics*, vol. 30, no. 11, pp. 6097–6107, Nov. 2015.

[18] S. Babic, F. Sirois, C. Akyel, G. Lemarquand, V. Lemarquand, and R. Ravaud, "New formulas for mutual inductance and axial magnetic force between a thin wall solenoid and a thick circular coil of rectangular cross-section," in *IEEE Transactions on Magnetics*, vol. 47, no. 8, pp. 2034–2044, Aug. 2011.

[19] H. Tavakkoli, E. Abbaspour-Sani, A. Khalilzadegan, A.-M. Abazari, and G. Rezazadeh, "Mutual inductance calculation between two coaxial planar spiral coils with an arbitrary number of sides," in *Microelectronics Journal*, vol. 85, pp. 98–108, 2019.

[20] Z. Luo and X. Wei, "Analysis of square and circular planar spiral coils in wireless power transfer system for electric vehicles," in *IEEE Transactions on Industrial Electronics*, vol. 65, no. 1, pp. 331–341, 2018.

[21] X. Zhang, C. Quan, and Z. Li, "Mutual inductance calculation of circular coils for an arbitrary position with electromagnetic shielding in wireless power transfer systems," in *IEEE Transactions on Transportation Electrification*, vol. 7, no. 3, pp. 1196–1204, Sept. 2021.

[22] Z. Dong, X. Li, S. Liu, Z. Xu, and L. Yang, "A novel all-direction antimisalignment wireless power transfer system designed by truncated region eigenfunction expansion method," in *IEEE Transactions on Power Electronics*, vol. 36, no. 11, pp. 12456–12467, Nov. 2021.

[23] J. Yi, P. Yang, Z. Li, P. Kong, and J. Li, "Mutual inductance calculation of circular coils for an arbitrary position with a finite magnetic core in wireless power transfer systems," in *IEEE Transactions on Transportation Electrification*, vol. 9, no. 1, pp. 1950–1959, Mar. 2023.

[24] Z. Lin, Z. Li, C. Hu, Z. Chen, and S. Huang, "Mutual inductance calculation method of arbitrarily positioned circular coils with convex ring type finite magnetic shielding in wireless power transfer," in *Transactions of China Electrotechnical Society*, vol. 39, no. 16, pp. 4918–4930, 2024.

[25] Y. Chen, K. Chen, S. Zheng, Y. Jiang, L. Yuan, and Z. Zhao, "Analytical modeling method for inductance of planar magnetic coupler in wireless power transfer," in *Proceedings of the CSEE*, vol. 43, no. 4, pp. 1504–1517, 2023.

[26] S. Dong, B. Wei, and B. Song, "An extensively applicable equivalent air gap method for mutual inductance calculation between coils with finite magnetic cores in wpt systems," in *IEEE Journal of Emerging and Selected Topics in Power Electronics*, vol. 13, no. 3, pp. 3966–3975, Jun. 2025.

[27] Y. Wu, Y. Jiang, Y. Li, H. Yuan, X. Wang, and Y. Tang, "Precise parameterized modeling of coil inductance in wireless power transfer systems," in *IEEE Transactions on Power Electronics*, vol. 39, no. 9, pp. 11746–11757, Sept. 2024.

[28] Z. Chen, Z. Li, M. Lyu, Z. Lin, and J. Li, "Coupling coefficient calculation method of circular coil with bilateral finite magnetic shields cat horizontal misalignment in wireless power transfer systems," in *International Journal of Circuit Theory and Applications*, vol. 53, no. 1, pp. 101–118, 2025.

Pengjie Gui was born in China in 2003. He received a bachelor's degree in electrical engineering and automation from Changsha University, Changsha, China, in 2017. He is currently working toward the master's degree in electronic information with Hunan University of Technology. His current research interests include wireless power transfer systems.

Zhiyuan Lin was born in China in 1996. He received the bachelor's degree in electronic information engineering from Hubei University of Technology Engineering and Technology College, Wuhan, China, in 2015, and the master's degree in electronic information from Hunan University of Technology in 2024. His current research interests include wireless power transfer systems.

Zhongqi Li was born in China in 1985. He received the M.Sc. degree from Hunan University of Technology, China, in 2012, and the Ph.D. degree from Hunan University in 2016. From 2016, he been working as an assistant professor at Hunan University of Technology, China. From 2020, he is now working as a postdoctoral fellow at Hunan University. His research interests include wireless power transfer systems and soft-switching power converters.